Table 2: AIC values for the models.

Subject	3-Parameters	*p*-fixed	V_A-fixed (0.15)	V_A-ignored
1	484. ± 20.	519. ± 28.	499. ± 15.	494. ± 15.
2	474. ± 9.	486. ± 14.	474. ± 9.	477. ± 8.
3	525. ± 12.	523. ± 8.3.	527. ± 10.	527. ± 7.
4	483. ± 14.	497. ± 21.	501. ± 12.	506. ± 13.
5	497. ± 18.	502. ± 19.	508. ± 32.	499. ± 13.
6	496. ± 11.	507. ± 14.	500. ± 9.	497. ± 9.

3-Parameters: Three parameters of K_1 and k_2, V_A were computed, p-fixed: K_1 and V_A was computed with fixing k_2 so as to p=K_1/k_2 =0.35 ml/g, V_A-fixed: K_1 and k_2 were computed with fixing V_A at 0.15 ml/g, V_A-ignored: K_1 and k_2 were computed without taking into account V_A.

Table 3: Values of K_1, $k2 \cdot p_{phys}$ and V_A (n=6) in whole and cortical region calculated by the present method for baseline and enalapril administrated conditions.

	K_1 (ml/min/g)	$k_2 \cdot p_{phys}$ (ml/min/g)	V_A (ml/ml)	*GFR* (ml/min/g)
Whole region				
Baseline	1.09 ± 0.33	3.11 ± 1.48	0.15 ± 0.09	0.35 ± 2 #
Enalapril	1.03 ± 0.44	2.55 ± 1.29	0.16 ± 0.14	
Cortical region				
Baseline	1.57 ± 0.60*	3.64 ± 2.15*	0.18 ± 0.12*	
Enalapril	1.42 ± 0.39*	3.55 ± 1.64*	0.25 ± 0.14*	

No significant difference was found between baseline and stimulated conditions. * Difference was significant between whole and cortical regions. # kidney weight of 300 g and cortex ratio of 70 % were assumed.

Figure Captions:

Fig. 1: Schematic diagram of the presnet computation procedure by the basis function method (BFM).

Fig. 2: Relationships of the regional ROI values of (A) K_1, (B) k_2 and (C) RBV by ROI based non-linear fitting method and pixel based BFM. The regression lines were, $K_{1,BFM}$ = 0.93 $K_{1,NLF}$ -0.11 ml/min/g (r = 0.80, P< 0.001), $k_{2,BFM}$ = 0.96 $k_{2,NLF}$ -0.13 ml/min/g (r = 0.77, P< 0.001) and $V_{A,BFM}$ = 0.92 $V_{A,NLF}$ -0.00 ml/ml (r = 0.97, P< 0.001), for K_1, k_2 and V_A, respectively.

Fig 3: Fitted curves to measured tissue TAC (plot) by the different computation methods. 3-Parameters: Three parameters of K_1, k_2 and V_A were computed, p-fixed: K_1 and V_A were computed with fixing $p(=K_1/k_2)$ at 0.35 ml/g, V_A-fixed: K_1 and k_2 were computed with fixing V_A at 0.15 ml/g, V_A-ignored: K_1 and k_2 were computed without taking into account V_A.

Fig. 4: Representative parametric images of K_1 (right) and $k2 \cdot p_{phys}$ (left) for one subject under the baseline condition. Coronal (upper) and transverse (lower) views are shown.

Fig. 5: Error propagation from the error in input delay time (a) and dispersion time constant (b) to K_1 and k_2 (two lines were identical). Positive and negative values of error indicate over- and under-correction of delay time and dispersion time, respectively.

Fig. 6: Error propagation from the partition coefficient (p ml/g) to K_1 and k_2. When the true p was varied between 0.6 and 0.8 ml/g, the size of error in RBF was simulated assuming p=0.7 ml/g.

Fig. 7: (a) Error propagation from the arterial blood volume (V_A ml/ml) to K_1 and k_2 (two lines were identical). When the true V_A changed from 0.0 to 0.4 ml/ml, the size of error in the K_1 and k_2 calculated, assuming V_A =0.0 ml/ml, was simulated. (b) Error propagation from the change of arterial blood volume from 0.14 ml/ml (ΔV_A) to the change in K_1 and k_2 from the initial condition (ΔK_1 and Δk_2 ml/min/g) (two lines were identical).

Figure 1

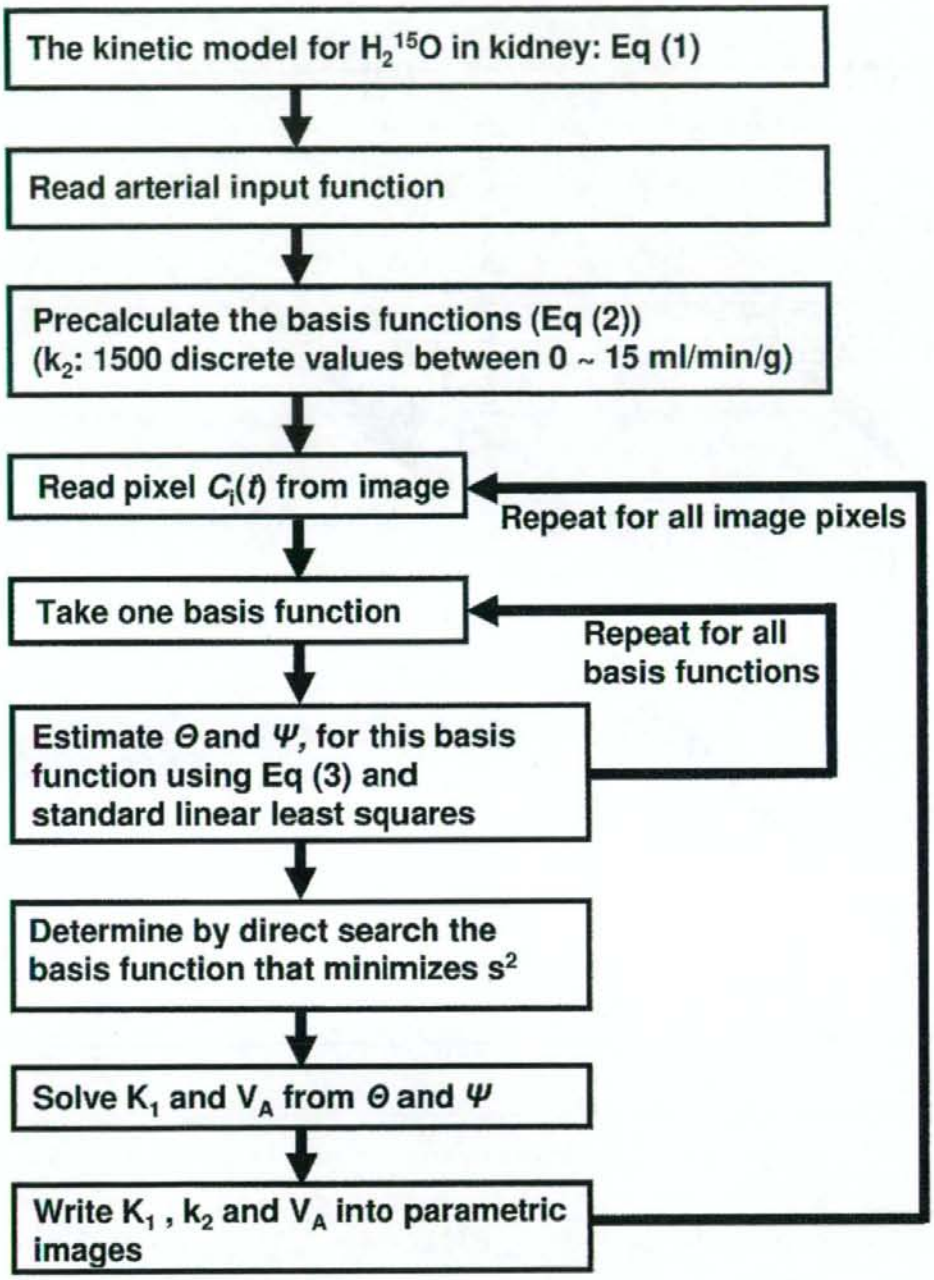
The kinetic model for $H_2{}^{15}O$ in kidney: Eq (1)
Read arterial input function
Precalculate the basis functions (Eq (2))
(k_2: 1500 discrete values between 0 ~ 15 ml/min/g)
Read pixel $C_i(t)$ from image
Repeat for all image pixels
Take one basis function
Repeat for all basis functions
Estimate Θ and Ψ, for this basis function using Eq (3) and standard linear least squares
Determine by direct search the basis function that minimizes s^2
Solve K_1 and V_A from Θ and Ψ
Write K_1 , k_2 and V_A into parametric images

Figure 2

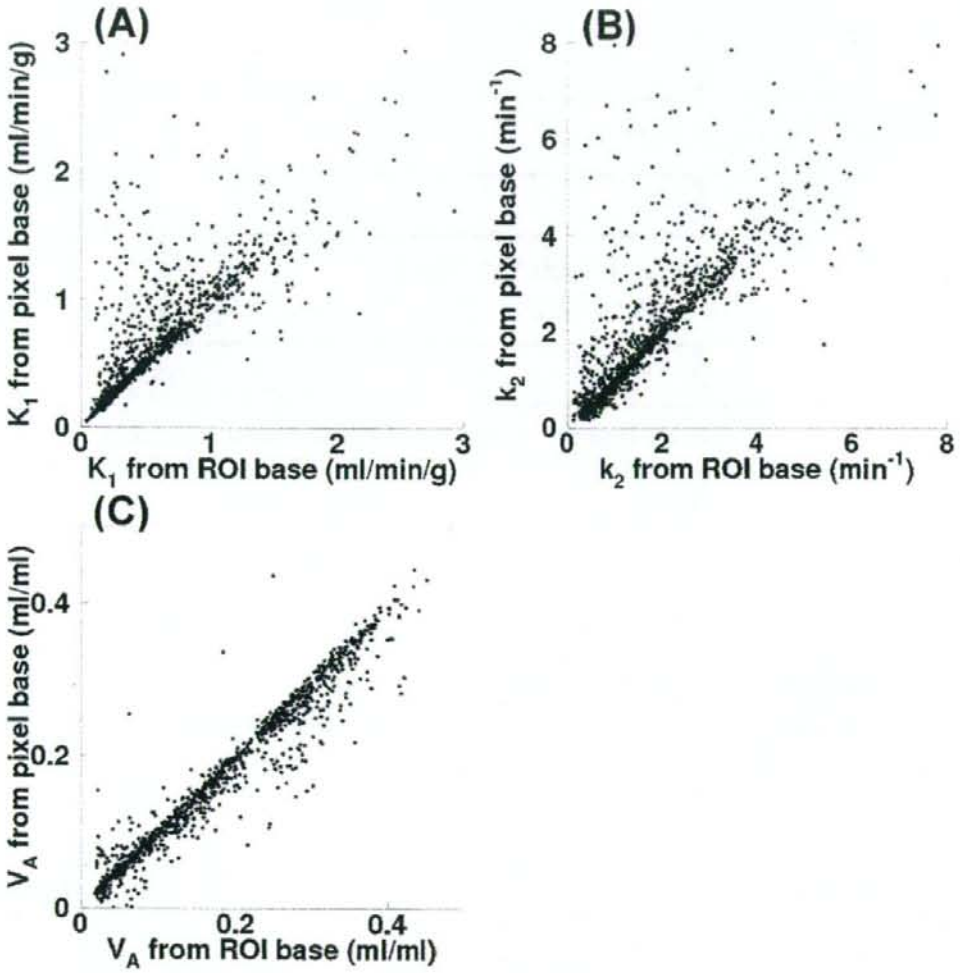
(A)
K1 from pixel base (ml/min/g)
K1 from ROI base (ml/min/g)
0
1
2
3
(B)
k2 from pixel base (min-1)
k2 from ROI base (min-1)
0
2
4
6
8
(C)
VA from pixel base (ml/ml)
VA from ROI base (ml/ml)
0
0.2
0.4

Figure 3

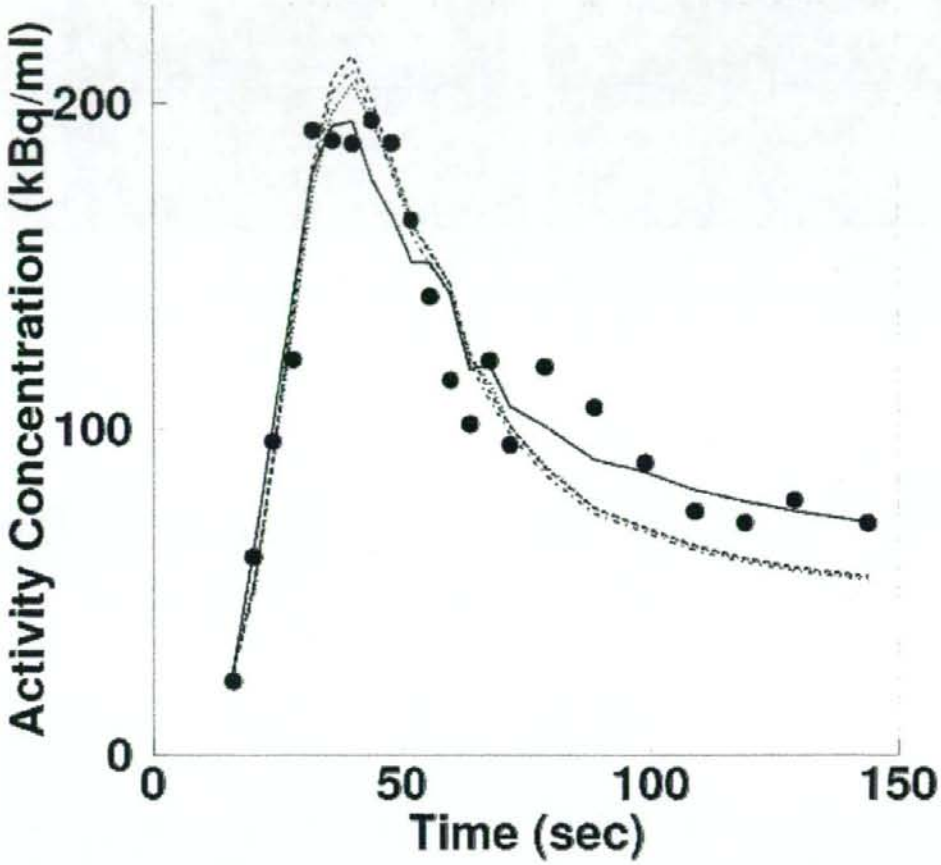

Figure 4

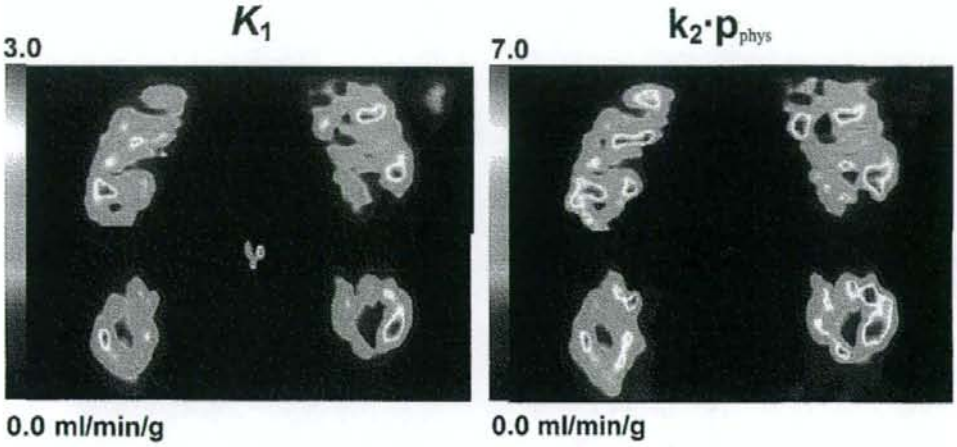

Figure 5

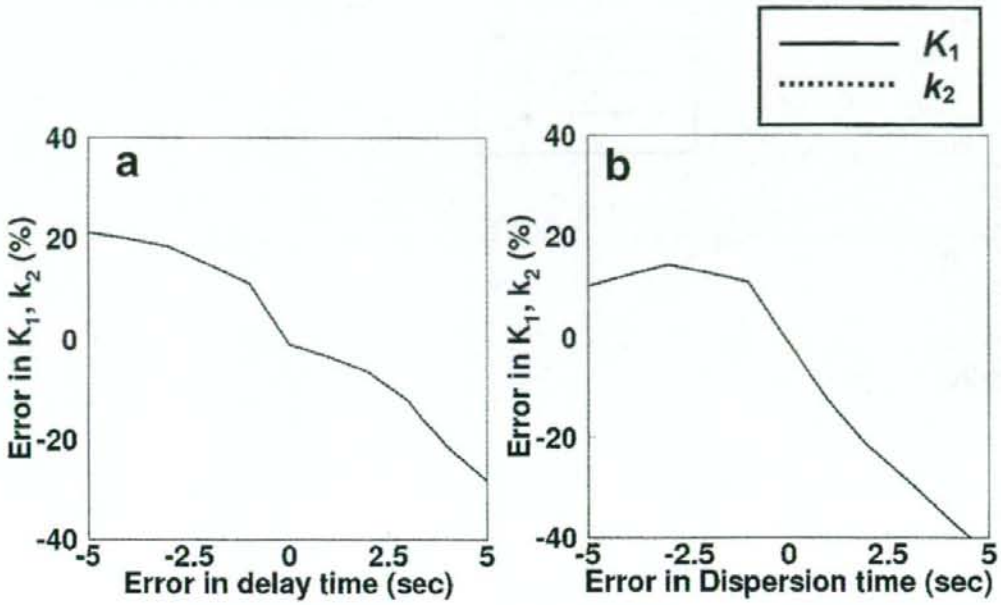
K_1
k_2
a
b
40
20
0
-20
-40
Error in K_1, k_2 (%)
-5
-2.5
0
2.5
5
Error in delay time (sec)
Error in Dispersion time (sec)

Figure 6

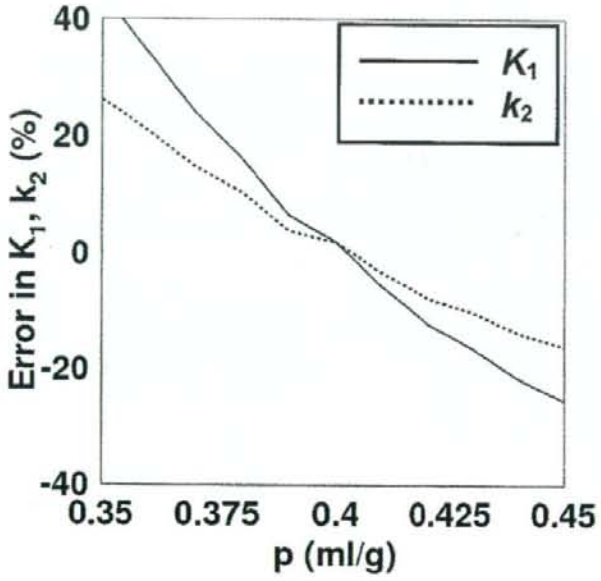

Figure 7

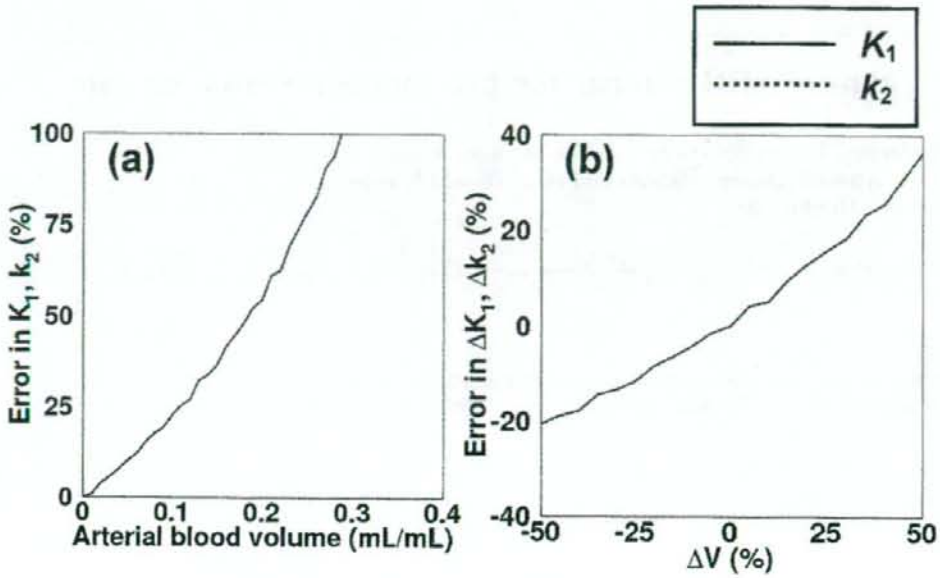
K_1
k_2
(a)
Error in K_1, k_2 (%)
100
75
50
25
0
0
0.1
0.2
0.3
0.4
Arterial blood volume (mL/mL)
(b)
Error in ΔK_1, Δk_2 (%)
40
20
0
-20
-40
-50
-25
0
25
50
ΔV (%)

Radiol Phys Technol
DOI 10.1007/s12194-008-0038-x

Use of a clinical MRI scanner for preclinical research on rats

Akihide Yamamoto · Hiroshi Sato · Jun-ichiro Enmi · Kenji Ishida · Takayuki Ose · Atsuomi Kimura · Hideaki Fujiwara · Hiroshi Watabe · Takuya Hayashi · Hidehiro Iida

Received: 27 May 2008 / Revised: 22 August 2008 / Accepted: 27 August 2008
© Japanese Society of Radiological Technology and Japan Society of Medical Physics 2008

Abstract This study evaluated the feasibility of imaging rat brains using a human whole-body 3-T magnetic resonance imaging (MRI) scanner with specially developed transmit-and-receive radiofrequency coils. The T_1- and T_2-weighted images obtained showed reasonable contrast. Acquired contrast-free time-of-flight magnetic resonance angiography images clearly showed the cortical middle cerebral artery (MCA) branches, and interhemispheric differences could be observed. Dynamic susceptibility contrast MRI at 1.17 mm^3 voxel resolution, performed three times following administration of gadolinium diethylenetriamine pentaacetic acid (Gd-DTPA, 0.1 mmol/kg), demonstrated that the arterial input function (AIF) can be obtained from the MCA region, yielding cerebral blood flow (CBF), cerebral blood volume, and mean transit time (MTT) maps. The hypothalamus (HT) to parietal cortex (Pt) CBF ratio was 45.11 ± 2.85%, and the MTT was 1.29 ± 0.40 s in the Pt region and 2.32 ± 0.17 s in the HT region. A single dose of Gd-DTPA enabled the assessment of AIF within MCA territory and of quantitative CBF in rats.

Keywords Quantitative mapping · Human whole-body 3-T MRI scanner · Single dose of Gd-DTPA · Dynamic susceptibility contrast (DSC) · Preclinical research · Rat brain

A. Yamamoto · J. Enmi · K. Ishida · T. Ose · H. Watabe · T. Hayashi · H. Iida (✉)
Department of Investigative Radiology,
Advanced Medical Engineering Center,
National Cardiovascular Center Research Institute,
5-7-1, Fujishiro-dai, Suita, Osaka 565-8565, Japan
e-mail: iida@ri.ncvc.go.jp

A. Yamamoto · A. Kimura · H. Fujiwara · H. Watabe · T. Hayashi · H. Iida
Department of Medical Physics and Engineering,
Division of Health Sciences, Graduate School of Medicine,
Osaka University, 1-7, Yamada-oka, Suita,
Osaka 565-0871, Japan

H. Sato
Laboratory for Diagnostic Solution,
Advanced Medical Engineering Center,
National Cardiovascular Center Research Institute,
5-7-1, Fujishiro-dai, Suita, Osaka 565-8565, Japan

1 Introduction

Magnetic resonance imaging (MRI) has been widely used in preclinical research on experimental small animals. Studies have typically been aimed at understanding the pathophysiologic status and evaluating the efficacy/side effects of newly developed treatments, such as pharmaceutical and regenerative medicine. Recently, a different idea has surfaced: the use of a human whole-body MRI scanner for small-animal imaging [1]. Although small-animal-dedicated scanners are superior to clinical scanners in terms of providing a better signal-to-noise ratio, the available pulse sequences are different from those in clinical scanners, and the magnetic field strength is often much higher. Small-animal imaging with clinical scanners is important for directly addressing clinical questions and/or identifying the origins of signal changes, including various disease conditions in a clinical setting.

Smith et al. [2] demonstrated that anatomic brain T_1- weighted (T_1W) images and T_2-weighted (T_2W) images can be obtained for healthy rats by using a 1-T clinical MRI scanner with a specially designed radiofrequency (RF) coil, given a reasonable spatial resolution (0.1953 × 0.1953 × 2.5 mm, 24 min of T_1W and 48 min of T_2W). The image contrast was sufficiently high to

distinguish the cortical gray matter from the white matter [corpus callosum (CC)], as well as the lateral ventricle (LV) and interpeduncular cistern (IPC) from the thalamus (Thal). Guzman et al. [3] employed a clinical 1.5-T MRI scanner with a commercially available RF coil and demonstrated that both T_1W and T_2W images can be obtained with good contrast, a reasonable spatial resolution of 0.3125 × 0.3125 × 1.5 mm, and an acquisition time of 19 min 51 s, as well as 0.35156 × 0.375 × 1.5 mm at 8 min 34 s, corresponding to T_1W and T_2W images, respectively. Other investigators [4] applied a clinical 1.5-T MRI scanner with a 3-in.-diameter circular receive-only surface coil to assess anatomic images. Their images can be used to evaluate the pathophysiologic status of stroke [4] and cancer [5, 6], as well as the effects of neural excitotoxicity [3]. There were also several studies that used a clinical 3-T MRI scanner fitted with commercial and/or hand-made RF coils to investigate the pathophysiology of stroke [7, 8] and brain tumors in rats [6, 9, 10]. Generally speaking, anatomic images with better contrast can be obtained in a stronger magnetic field, although there are additional factors that may influence the signal-to-noise ratio (SNR) or spatial resolution of anatomic images. Contrast-free time-of-flight magnetic-resonance angiography (TOF-MRA) can also be performed on rats; a reasonable spatial resolution was obtained by using a clinical 3-T MRI scanner with a single-turn solenoid coil [11].

Dynamic susceptibility contrast MRI (DSC-MRI) [12] has been widely used in clinical diagnosis, particularly in patients with stroke [13–19] and tumors [20]. The application of clinical MRI scanners has been extended to DSC-MRI studies of small animals with stroke [21, 22] and tumors [23] using a 1.5-T MRI scanner. Up to now, small-animal studies have been performed on 1.5-T MRI scanners only, and 3-T scanners have not been employed so far. This is largely attributed to the fact that the susceptibility-induced inhomogeneous magnetic field can cause more serious distortion of the images at a higher static magnetic field. In DSC-MRI studies, the echo planar imaging (EPI) technique is mainly used because fast acquisition is required for accurate tracking of the bolus passage of MR contrast agents. The EPI technique, however, is very sensitive to magnetic field inhomogeneity, and thus the EPI images of small-animal brains may be severely distorted. The gradient slew rate (SR) is not high enough to support a sufficiently short echo spacing period when clinical scanners are used for high spatial resolution imaging of small objects. Moreover, injected materials may cause further distortion [24]. The degree of distortion of dynamic EPI images of small-animal brains produced by a 3-T clinical scanner is currently unknown. The arterial input function (AIF) is also questionable. To the best of our knowledge, no DSC-MRI studies of small-animal brains on 3-T clinical scanners have been reported.

This study attempted to evaluate the feasibility of developing a human whole-body 3-T MRI system for small animals, particularly DSC-MRI with a single dose of gadolinium-diethylenetriamine pentaacetic acid (Gd-DTPA). The quality of various images—including the anatomic T_1W images, T_2W images, time-of-flight magnetic resonance angiography (TOF-MRA) images and DSC images—was tested, and the availability of the AIF obtained from rat brain was evaluated.

2 Materials and methods

2.1 Subjects

The subjects were three healthy adult rats supplied by Japan SLC, Inc. (Shizuoka, Japan). All three rats were males, and they ranged in age from 20 to 24 weeks. Their weight range was between 400 and 600 g. Anesthesia was administered with an intramuscular injection of ketamine (33 mg/kg; Daiichi-Sankyo Co., Ltd., Tokyo, Japan) and xylazine (6.6 mg/kg; Bayer Yakuhin, Ltd., Osaka, Japan). The first rat (Sprague Dawley, SD) was used for T_1-W and T_2W imaging of the whole brain. The second rat, also a SD, was used for contrast-free TOF-MRA imaging. The third was a Wistar rat, which was used for a Gd-DTPA (0.1 mmol/kg; Bayer Yakuhin, Ltd., Osaka, Japan)-enhanced DSC-MRI sequence. Experiments were carried out according to the protocol approved by the Local Committee for Laboratory Animal Welfare, National Cardiovascular Center, Osaka, Japan.

2.2 MRI acquisition

A human whole-body 3-T MRI scanner (Signa, GE Healthcare, Milwaukee, WI, USA) equipped with a 55-cm bore was employed in this study. The gradient coil system was capable of providing a maximum gradient amplitude of 40 mT/m and an SR of 150 T m^{-1} s^{-1}. All sequence programs employed in this study were designed for clinical studies.

Two solenoid coils designed for rats were specially developed to cover the whole brain, and were capable of both transmitting and receiving RF pulses. The three-turn solenoid coil, which had a diameter of 42 mm and a length along its cylindrical axis of 18 mm, was attached to an apparatus made from an acrylic mold, as shown in Fig. 1. All components of the stereotaxic apparatus consisted of nonmagnetic materials that fixed the head positions of the rats during data acquisition. The RF coil was designed to have an impedance of 50 Ω at a resonance frequency of

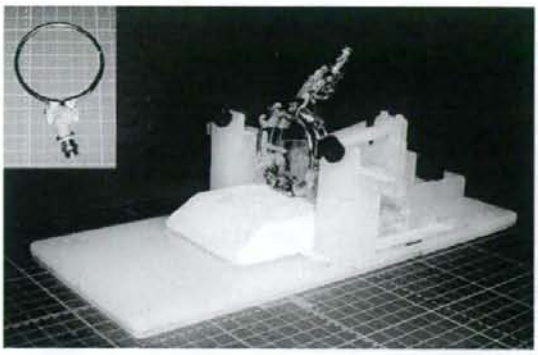

Fig. 1 The head fixation system for small animals, which was fitted with an MRI coil for RF transmission and reception. The coil is typically a three-turn solenoid; it can also be a single-turn coil, as shown on the *top left* of this figure

127.76 MHz. An additional single-turn surface coil of diameter 62 mm diameter was also developed for better homogeneity and was used for a single slice of DSC-MRI. The RF power in these coils had to be reduced to less than that used in the standard human head coil because of the diameter of the small coil. The transmission signal was therefore attenuated to 20 dB, which allowed the use of automated scanner software, including the calibration of the RF transmission power and receiver gains. All rats were fixed on the stereotaxic apparatus. They were placed at the center of the gantry and oriented with the craniocaudal axis perpendicular to the static magnetic field. Their heads were positioned inside the coil along the craniocaudal direction.

T_1W images were obtained with a conventional two-dimensional fast spin echo (2D-FSE) sequence. The repetition time (TR) was 1,500 ms [10]. The echo time (TE) was fixed at 14 ms. The echo train length (ETL) was 3. The field of view (FOV) was set at 40 × 30 mm^2, the slice thickness at 1.5 mm, the slice gap at 0.5 mm, the number of excitations (NEX) at 10, and the band width (BW) at 31.3 kHz. The acquired matrix (256 × 160) was interpolated, and null pixels were added in k-space to produce square matrices of 256 × 256. The acquisition time was 10 min 3 s.

T_2W images were obtained with a 2D-FSE and the following imaging parameters: TR, 4,100 ms; TE, 128 ms; ETL, 14; FOV, 40 × 30 mm; slice thickness, 1.5 mm; slice gap, 0.5 mm; NEX, 8; BW, 31.3 kHz; acquired matrix, 256 × 160, zero-filled to 256 × 256; phase direction, ventral-dorsal; acquisition time, 11 min 2 s.

Time-of-flight magnetic resonance angiography was performed using a three-dimensional flow-compensated spoiled gradient recalled (3D-SPGR) sequence prepared with magnetization transfer and with: TR, 53 ms; TE, 5.5 ms; flip angle (FA), 45°; BW, 16 kHz; FOV, 8 × 6 cm; slice thickness, 0.2 mm; one acquired slab of 512 × 512 × 64; voxel resolution, 0.156 × 0.156 × 0.2 mm^3; NEX, 1; acquisition time, 21 min 46 s.

Dynamic susceptibility contrast images were obtained following the intravenous administration of Gd-DTPA to the T_2*-weighted gradient echo dynamic images. A bolus of Gd-DTPA (0.1 mmol/kg) was injected manually into the tail vein with a 22-gauge catheter via 1 m of polyethylene tubing (PE50, internal diameter: 0.58 mm/outer diameter: 0.965 mm, Becton Dickinson and Company, Franklin Lakes, NJ, USA), and was followed by an additional administration of saline (1.0 ml). A multishot EPI (number of shots = 2) was employed to improve EPI distortion and temporal resolution. The imaging parameters were: TR, 142 ms; TE, 22.1 ms; FA, 20°; FOV, 40 × 40 mm; matrix size, 64 × 64, leading to a pixel size of 0.625 × 0.625 mm^2. The slice thickness was 3 mm in a single slice around the hypothalamus (HT). The temporal resolution was 0.284 s per image, and the acquisition time was 1 min 15 s. This assessment was repeated three times at intervals of 40 min and 10 min, corresponding to the first–second and second–third scans, respectively.

2.3 Data analysis

All MRI images were reconstructed on the same workstation provided for the GE Signa 3-T scanner used for the clinical programs. The images were then transferred to a Linux workstation. Lastly, data analysis was carried out using in-house and commercial software.

To evaluate the T_1W and T_2W image quality, we calculated the contrast-to-noise ratio (CNR) with an inter-tissue method [25–27] as follows: $CNR = (\pi/2)^{1/2} (SI_a - SI_b)/SI_{air}$, where SI_{air} represents the mean signal intensity of air, and SI_a and SI_b represent the signal intensities of tissue a and tissue b, respectively.

Angiograms were created by generating the partial maximum intensity projection (MIP) with commercial software [Virtual Place Liberty (VPL), AZE Co. Ltd., Tokyo, Japan]. Visible middle cerebral artery (MCA) branches and left-to-right differences in MCA were carefully investigated.

For the DSC images of slice sections containing the internal carotid artery (ICA) and/or MCA, a series of images were carefully observed. A region of interest (ROI) was carefully selected in the MCA region, from which the AIF was obtained, with the help of other anatomic information. To avoid susceptibility artifacts caused by air in the trachea, the area of the arterial circle of Willis was excluded from the definition of the AIF. The anterior cerebral artery was also excluded because of possible susceptibility effects attributed to venous blood. A Gaussian filter of full width at half maximum (FWHM) 1.1 mm

was applied to all dynamic images. The time versus signal intensity curves (TICs) were converted to the Gd-DTPA concentration according to Eq. 1 given in the "Appendix." Functional mapping images of the mean transit time (MTT), cerebral blood volume (CBV), and cerebral blood flow (CBF) were carried out with the deconvolution method [28]. The theory behind this is described in detail in the "Appendix." For ROI analysis, images of matrix size 64 × 64 were converted to 256 × 256 using a sinc interpolation function.

3 Results

T_1W and T_2W images reconstructed with a spatial resolution of 0.156 × 0.188 × 1.5 mm are shown in Fig. 2. White matter could be discriminated from cortical and deep gray matter regions. The locations of small anatomic features such as the caudate putamen (CPu), striatum, the CC, and the hippocampus (HC) could also be identified in both T_1W and T_2W anatomic images. The CNRs between the HC and CC were 15.6 and 9.8, respectively, for the T_1W and T_2W images shown in Fig. 2. The CNRs between the HC and IC were 23.2 and 13.6, respectively, although the CNR may be underestimated due to the contamination of signal from the globus pallidus.

Results for MIP images obtained with contrast-free TOF-MRA are shown in Fig. 3. Coronal MIP images around the HT of thickness 5 mm are shown in Fig. 3a. In this figure, the slice section contained ICAs and MCA. The MCA, the cortical branches in both the left and right hemispheres, can be identified. It is important to note that the anatomic structure of the cortical MCA arteries is different between the right and left hemispheres. The ROI for the AIF was selected in the MCA region and is shown by the arrows in Fig. 3a and b.

A typical example of a DSC-MRI image is shown in Fig. 4. Distortion of the DSC-MRI images is visible in Fig. 4A in the phase direction. A magnified area from dynamic images of the MCA region (shown as a rectangle in Fig. 4A) is displayed in Fig. 4B. Several pixels indicate temporal changes in pixel contrast as a function of time, and these are reflected by Gd-DTPA negative enhancement. The pixel signal intensity varied as shown in Fig. 4C, and the curve shown was employed to estimate the AIF. Figure 5 shows the TIC in this area together with the TIC for the whole brain region obtained from each of the three scans. The curves were visually reproducible in terms of the shapes, heights and widths of the curves around the peak, as well as the tail height at the end of the scan. It should also be noted that the baseline was consistent before each injection of Gd-DTPA, even though the second and

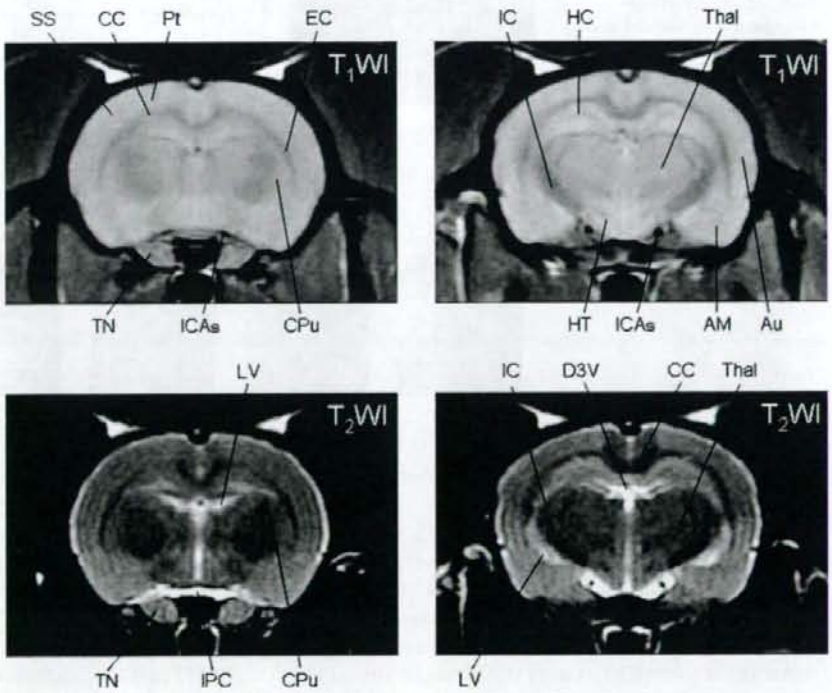

Fig. 2 T_1W images (*top*) and T_2W images (*bottom*) obtained from an SD rat, with the following anatomic locations as indicated: the somatosensory cortex (*SS*), corpus callosum (*CC*), parietal cortex (*Pt*), external capsule (*EC*), caudate putamen (*CPu*), internal capsule (*IC*), hippocampus (*HC*), thalamus (*Thal*), auditory cortex (*Au*), amygdala (*AM*), hypothalamus (*HT*), internal carotid arterial system (*ICAs*), trigeminal nerve (*TN*), interpeduncular cistern (*IPC*), dorsal third ventricle (*D3V*), and the lateral ventricle (*LV*). These slice sections were located −1.5 mm (*left*) and −3.5 mm (*right*), respectively, from the bregma

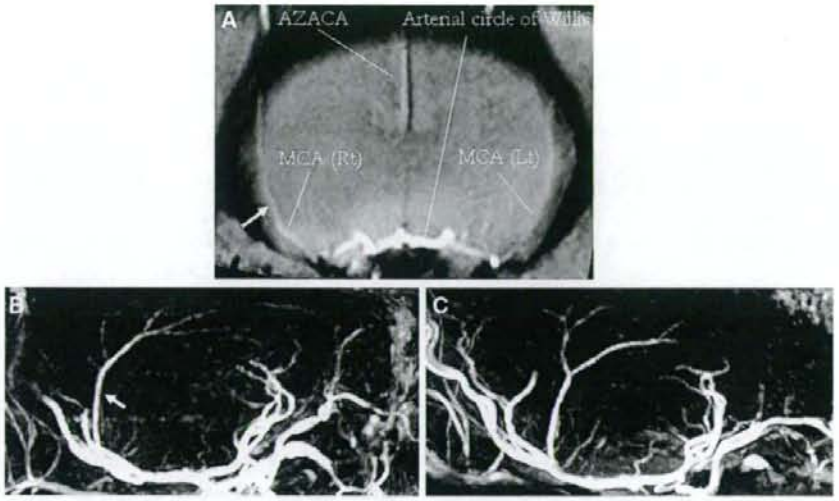

Fig. 3 Partial maximum intensity projection maps of contrast-free time-of-flight MRA obtained for a Sprague Dawley rat. Maps represent areas around the Thal (**a**), right hemisphere (**b**), and left hemisphere (**c**). The *white arrows* indicate the selected ROI level (as described in the "Discussion"). *AZACA*, azygos anterior cerebral artery

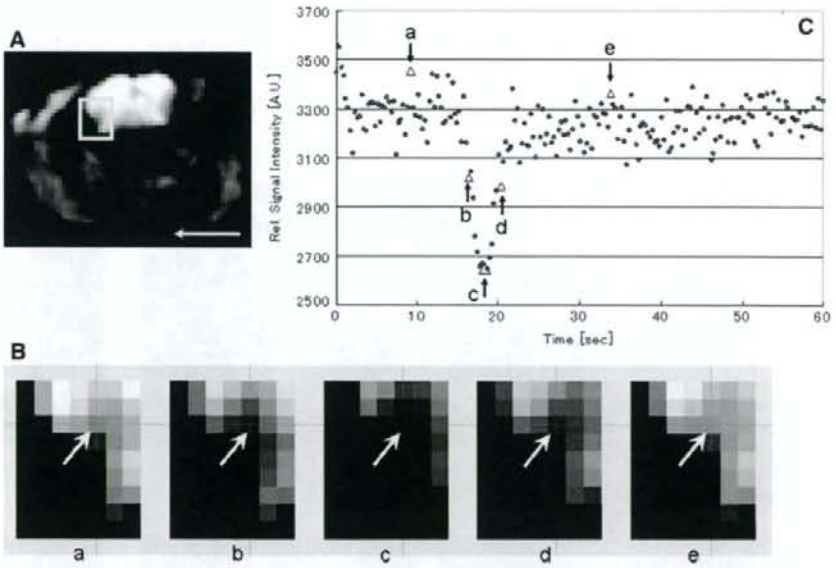

Fig. 4 Typical time-frame images obtained from Gd-bolus tracking T_2*-weighted dynamic images (after the first injection). A *white rectangle* was placed in the MCA area (**a**), and magnified images of this rectangle were visualized as *a*, *b*, *c*, *d*, and *e* in **b**. The TIC within the pixels is indicated by *white arrows* in **b**. The data were then plotted in a graph (**c**). Typical data points were extracted from the first injection at the times of 9.2 (*a*), 16.4 (*b*), 18.1 (*c*), 20.1 (*d*), and 33.9 (*e*) s. The phase direction is shown as a *white arrow* in **a**

the third curves should have been affected by the previous injection of Gd-DTPA.

Functional mapping images of CBF, CBV, and MTT calculated according to the theory described in the "Appendix" are shown in Fig. 6. Images obtained from this sequential assessment appeared to be reasonably clear, although slightly noisy, and were consistent among the scans. The absolute CBFs (mean ± SD) in the cortical gray matter area (mainly the parietal cortex, Pt) were 24.04 ± 2.88, 17.75 ± 3.34, and 31.87 ± 7.27 ml g^{-1} min^{-1} for the first, second, and third scans, respectively. The HT-to-Pt CBF ratios were 46.7, 51.5, and 43.0% for the first, second, and third scans, respectively. The CBVs were 0.49 (0.44), 0.50 (0.35), and 0.47 (0.41) ml/ml in the Pt (the HT) region in the first, second, and third scans, respectively. The MTTs in the same regions were 1.22 (2.51), 1.72 (2.29),

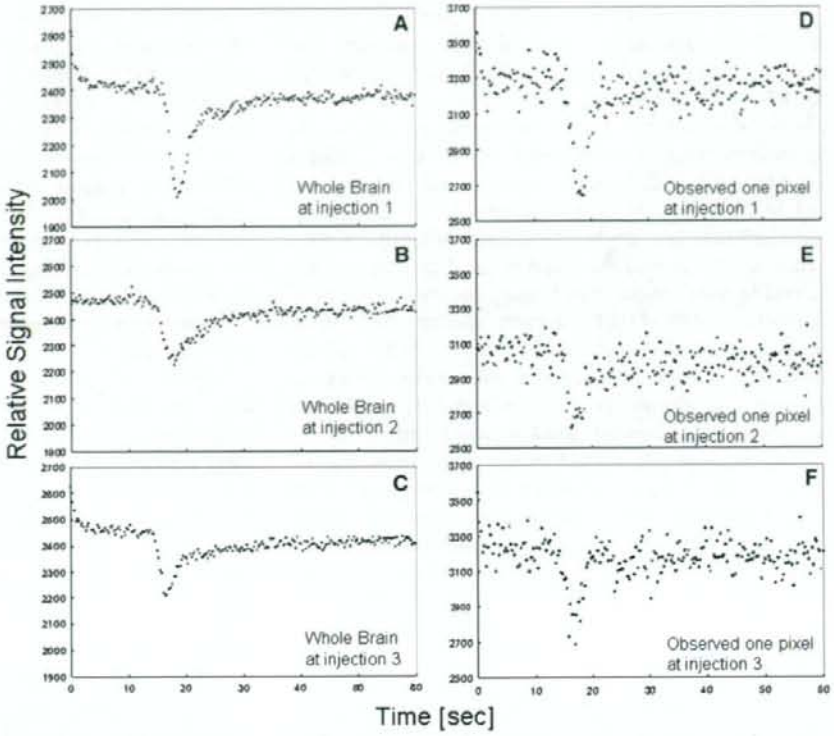

Fig. 5 TIC dynamic changes in the whole brain are shown in the first injection (**a**), the second injection (**b**), and the third injection (**c**). For each injection, a one-pixel ROI was selected and observed, as shown for the first (**d**), second (**e**) and third (**f**) injections, respectively. The negative enhancement changes in the rate from peak signal intensity to baseline were 16.8% (**a**), 10.0% (**b**), and 10.3% (**c**) at the whole brain (average 12.3, SD 3.9). The peak-to-base fractions at selected ROIs were 19.2% (**d**), 14.5% (**e**), and 16.9% (**f**) (average 16.9, SD 2.3), for the first, second, and third injections, respectively

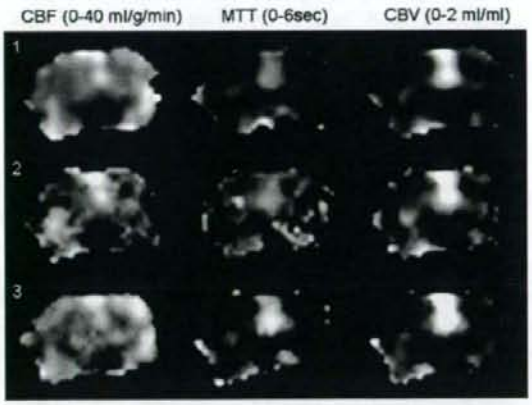

Fig. 6 *First column on the left*: CBF maps using the AIF from MCA, pictured in a grayscale from 0 to 4 ml g^{-1} min^{-1}. MTT maps are shown in the *middle column*, followed by CBV maps of 0–2 ml g^{-1} min^{-1} in the *column on the right*. Deconvolution was carried out pixel by pixel with b-SVD and then smoothed to 0.15625 × 0.15625 mm in-plane resolution from the acquired voxel resolution of 0.625 × 0.625 × 3 mm (1.17 mm^3) in DSC-MRI

and 0.92 (2.16) s in each of the three scans. Among the three injections, the absolute MTTs (mean ± SD) were 1.29 ± 0.40 s in the Pt and 2.32 ± 0.17 s in the HT region.

4 Discussion

This study demonstrated that our system of a human whole-body 3-T MRI fitted with an in-house solenoid coil developed for small animals can provide morphologic and functional images of the rat brain in vivo. The quality of T_1W and T_2W images obtained with a scan duration of approximately 10 min was better than those obtained in previous studies in which 1.5-T clinical MRI scanners [3] were employed. The neocortex and large subcortical structures, such as the Thal and HC, are readily recognized from their topographic relationship to the CC, the ventricular system, and the subarachnoid space [2]. In T_1W images, the cerebrospinal fluid (CSF)-containing spaces are visible as they are hypointense, and the arterial flow showed a signal loss caused by so-called flow void effects, which is typically seen in the spin echo sequence [2]. In T_2W images, the CSF was bright and white (prolonged T_2 relaxation time), whereas the myelinated white matter was black (short T_2 relaxation time). The white matter tracts such as the IC and CC were clearly visible in both T_1W and T_2W images, and better quality was obtained compared to previous reports employing 1.0- and 1.5-T clinical MRI scanners [2, 3].

Magnetic resonance angiography images also clearly showed the structure of the distal MCA branches. The MRA findings of interhemispheric differences with regards to MCA in the SD rat were also consistent with a previous report on Wistar rats [29], which indicated left-to-right asymmetric structure in three out of ten Wistar rats using a 7-T MRI scanner dedicated to small-animal imaging [29]. Our MRA images are superior to those obtained in previous work [11] that employed a clinical 3-T MRI scanner and that only showed the major cerebral arteries and the carotid arteries because they focused mainly on validating occlusion models [11]. The superior quality of our MRA images can largely be attributed to the type of RF coil we used. Ours is a three-turn solenoid coil that covers only the cerebral area, whereas the previous work [11] employed a single-turn coil (diameter of 6.4 cm and length of 10 cm) that covered the whole head, including the brain and the neck. Additionally, the prolonged acquisition period in our study (almost 20 min) compared to the acquisition period used in the previous study [11] (almost 4 min) may have been a factor that led to higher-quality MRA images.

An important point about this study is that DSC-MRI images of reasonable quality can also be obtained with a clinical MRI scanner at 3 T on rats. In addition, we were able to extract the AIF from the rat brain, which is an important accomplishment. Selection of an ROI in the MCA region successfully provided the AIF. Spatial distortion or susceptibility artifacts were not visible in our observations. Signal changes were obtained during DSC-MRI following a single dose of Gd-DTPA. During this study, the dedicated transmit and receive RF coils were considered to be crucial to obtaining a reasonable SNR. Our study was performed with the same sequence and the same dose rate (0.1 mmol/kg) of Gd-DTPA that are commonly used in clinical examinations. Moreover, it was performed with high ($1.17\ mm^3$)-resolution dynamic imaging.

The quantitative images of CBF were consistent with those in a previous report on the use of [^{14}C] iodoantipyrine [30]. Namely, the HT-to-Pt contrast in CBF was 43–52% in this study, which is close to the values reported by Bloom et al. [30] of 44–58%. Although the absolute CBF and CBV values in our study were different from those obtained previously [13, 30, 31], the uncertain scaling factors for each of these were canceled out when calculating the MTT with Eq. 5 [32] (see also the "Appendix"). The MTT obtained in this study was comparable to those obtained in previous work [31, 33].

We noticed that the absolute CBF and CBV values were overestimated, which suggests that some limitations apply, such as the partial volume effect (PVE) caused by insufficient spatial resolution as compared with the anatomic structure of the MCA. Detection of AIF with a repeat injection was performed (Fig. 5, right row). The major MCA diameter was approximately 0.5 mm at the maximum, as evaluated from Fig. 3, which suggested that the measured AIF is largely influenced by the PVE [24]. Also, the differences in absolute value may be due to the fact that a nonlinear relationship exists between the signal intensity and the contrast agent concentration. Previous reports have proposed nonlinearity correction methods for brain tissue [34] and AIF [35]. Further studies are needed to confirm the accuracy and the reproducibility [36]. Image distortion caused by dielectric effects [37] and/or EPI distortion [38] are other sources of error, and should be investigated systematically.

Improving the quality of the original dynamic images acquired would also improve the mapping image quality. In order to achieve better detection of the dynamic susceptibility contrast caused by T_2* signals, the optimization of TE, FA and the acquisition matrix should be investigated. We speculate that a multichannel phased array coil and parallel imaging techniques would reduce the level of distortion. The DSC-MRI in this study was obtained for only a single slice. Further careful attention is needed to perform multislice imaging in order to minimize inflow effects [35]. In our study, the contrast concentration $C(t)$ curves including the AIFs varied slightly among the three injections. A sophisticated injector system that is MR-compatible may improve the variation.

A dedicated high magnetic field scanner equipped with a dedicated small bore is the optimal device for small-animal imaging. However, such systems are not commonly available. The system developed in this study might serve as a low-cost solution or an alternative. The use of the present system provides an opportunity to use the same imaging platform available for clinical studies for small-animal imaging [7]. This would allow us to determine pathophysiological status from MRI signals using animal models with various diseases. More importantly, the optimization of several scan parameters, which has been difficult to achieve in clinical patients, can easily be performed on small animals with this system. In particular, the reproducibility of the assessment of CBF with DSC-MRI, which has been reported to be a limitation on clinical studies [19, 36], could be improved by performing a systematic evaluation of each scan parameter when this system is used on small animals rather than clinical patients. With the addition of a high-strength insert gradient coil [39], which allows for thinner slices and much faster read-out, the system performance and the spatial resolution with an acceptable SNR can be improved. The use of adapting coils could be an effective solution for those who operate MR scanners for human subjects and intend to gain experience [40] in preclinical research.

5 Conclusion

In this preclinical study on rats, reasonable image quality was obtained for T_1W, T_2W, and contrast-free TOF-MRA images generated using a human whole-body 3-T MRI scanner and a newly developed solenoid coil. In DSC-MRI, this system visualized transient signal changes with a single dose of Gd-DTPA and using the same sequences commonly used in clinical examinations. A human whole-body 3-T MRI scanner and dedicated coil make it possible to detect the AIF in the MCA region of Wistar rats. High-resolution DSC-MRI was accomplished with a clinical scanner, but the spatial resolution with an acceptable SNR was insufficient for the rat brain. Although there may be some remaining issues relating to AIF, we have shown the potential of DSC-MRI in our study.

Acknowledgments The authors would like to express our appreciation to the reviewers, the editors and the editorial assistants of *Radiological Physics and Technology* for their invaluable advice on how to improve our manuscript. This study was supported by a grant for research on Advanced Medical Technology from the Ministry of Health, Labor and Welfare, Japan. We would like to thank the VPL released by AZE Ltd. (Tokyo, Japan) and the software library provided by the Oxford University Center for Functional MRI of the Brain. We are grateful to the staff at the National Cardiovascular Center for their invaluable contributions and efforts. Last but not least, we would like to express our thanks to Miss Atra Ardekani (a summer intern from McGill University in Montreal, Quebec, Canada).

Appendix: Calculation of functional mapping images from DSC-MRI

The observed TIC $S(t)$ was converted to a time-versus-concentration curve (TCC) $C(t)$ by the following equation [16, 36]:

$$C(t) = k \cdot \Delta R2^*(t) = -k \cdot \ln(S(0)/S(t))/\mathrm{TE}, \quad (1)$$

where $\Delta R2^*$ is the change in the T_2^* relaxation rate and k is a constant. In this study, it was assumed that $k = 1$. $S(0)$ is the pre-contrast (baseline) signal and $S(t)$ is the measured signal at time t. The next step was to fit this first-pass period of TCC to a gamma variate function:

$$C(t) = a(t-b)^c \exp(-(t-b)/d), \quad (2)$$

where a, b, c, and d were determined by nonlinear least-squares fitting. To minimize the effects of the recirculation of the contrast agent, data were neglected in the fit if these concentrations were less than 50% of the maximum after the peak of the TCC.

The fitted tissue TCC $Ct(t)$ was deconvolved by the fitted AIF $C_{\mathrm{AIF}}(t)$ by using singular value decomposition with a block-circulant deconvolution matrix (b-SVD) method [28] according to the equation

$$\mathrm{CBF} \cdot R(t) = Ct(t) \otimes^{-1} C_{\mathrm{AIF}}(t), \quad (3)$$

where $\otimes^{-1}$ represents the deconvolution operator and $R(t)$ is a residue function representing the tissue response to an instantaneous bolus. CBF·$R(t)$ was estimated by deconvolving $Ct(t)$ by $C_{\mathrm{AIF}}(t)$ using b-SVD, and then CBF was determined as the maximum value of the obtained CBF·$R(t)$.

The CBV was calculated as follows:

$$\mathrm{CBV} = \int_0^\infty Ct(t)\mathrm{d}t \Big/ \int_0^\infty C_{\mathrm{AIF}}(t)\mathrm{d}t. \quad (4)$$

Lastly, the MTT is calculated from CBF and CBV by applying the central volume principle [32]:

$$\mathrm{MTT} = \mathrm{CBV}/\mathrm{CBF}. \quad (5)$$

References

1. Brockmann MA, Kemmling A, Groden C. Current issues and perspectives in small rodent magnetic resonance imaging using clinical MRI scanners. Methods. 2007;43:79–87.
2. Smith DA, Clarke LP, Fiedler JA, Murtagh FR, Bonaroti EA, Sengstock GJ, et al. Use of a clinical MR scanner for imaging the rat brain. Brain Res Bull. 1993;31(1–2):115–20.
3. Guzman R, Lövblad KO, Meyer M, Spenger C, Schroth G, Widmer HR. Imaging the rat brain on a 1.5 T clinical MR-scanner. J Neurosci Methods. 2000;97(1):77–85.
4. Fujioka M, Taoka T, Matsuo Y, Hiramatsu KI, Sakaki T. Novel brain ischemic change on MRI: delayed ischemic hyperintensity on T_1-weighted images and selective neuronal death in the caudoputamen of rats after brief focal ischemia. Stroke. 1999;30(5):1043–6.
5. Thorsen F, Ersland L, Nordli H, Enger PO, Huszthy PC, Lundervold A, et al. Imaging of experimental rat gliomas using a clinical MR scanner. J Neurooncol. 2003;63(3):225–31.
6. Biswas J, Nelson CB, Runge VM, Wintersperger BJ, Baumann SS, Jackson CB, et al. Brain tumor enhancement in magnetic resonance iimaging: comparison of signal-to-noise ratio (SNR) and contrast-to-noise ratio (CNR) at 1.5 versus 3 Tesla. Invest Radiol. 2005;40:792–7.
7. Shimamura M, Sato N, Sata M, Kurinami H, Takeuchi D, Wakayama K, et al. Delayed postischemic treatment with fluvastatin improved cognitive impairment after stroke in rats. Stroke. 2007;38:3251–8.
8. Lee JM, Zhai G, Liu Q, Gonzales ER, Yin K, Yan P, et al. Vascular permeability precedes spontaneous intracerebral hemorrhage in stroke-prone spontaneously hypertensive rats. Stroke. 2007;38:3289–91.
9. Wintersperger BJ, Runge VM, Biswas J, Reiser MF, Schoenberg SO. Brain tumor enhancement in mr imaging at 3 Tesla: comparison of SNR and CNR gain using TSE and GRE techniques. Invest Radiol. 2007;42:558–63.
10. Sato H, Enmi J, Teramoto N, Hayashi T, Yamamoto A, Tsuji T, et al. Comparison of Gd-DTPA-induced signal enhancements in rat brain C6 glioma among different pulse sequences in 3-Tesla magnetic resonance imaging. Acta Radiol. 2008;49:172–9.
11. Yang YM, Feng X, Yao ZW, Tang WJ, Liu HQ, Zhang L. Magnetic resonance angiography of carotid and cerebral arterial

occlusion in rats using a clinical scanner. J Neurosci Methods. 2008;167(2):176–83.
12. Rosen BR, Belliveau JW, Vevea JM, Brady TJ. Perfusion imaging with NMR contrast agents. Magn Reson Med. 1990;14(2):249–65.
13. Calamante F, Thomas DL, Pell GS, Wiersma J, Turner R. Measuring cerebral blood flow using magnetic resonance imaging techniques. J Cereb Blood Flow Metab. 1999;19(7):701–35.
14. Yamada K, Wu O, Gonzalez RG, Bakker D, Østergaard L, Copen WA, et al. Magnetic resonance perfusion-weighted imaging of acute cerebral infarction: effect of the calculation methods and underlying vasculopathy. Stroke. 2002;33(1):87–94.
15. Tamura H, Hatazawa J, Toyoshima H, Shimosegawa E, Okudera T. Detection of deoxygenation-related signal change in acute Ischemic stroke patients by T2*-weighted magnetic resonance imaging. Stroke. 2002;33(4):967–71.
16. Calamante F, Gadian DG, Connelly A. Quantification of perfusion using bolus tracking magnetic resonance imaging in stroke: assumptions, limitations, and potential implications for clinical use. Stroke. 2002;33(4):1146–51.
17. Latchaw RE, Yonas H, Hunter GJ, Yuh WT, Ueda T, Sorensen AG, et al. Guidelines and recommendations for perfusion imaging in cerebral ischemia: a scientific statement for healthcare professionals by the Writing Group on Perfusion Imaging, from the Council on Cardiovascular Radiology of the American Heart Association. Stroke. 2003;34(4):1084–104.
18. Carroll TJ, Rowley HA, Haughton VM. Automatic calculation of the arterial input function for cerebral perfusion imaging with MR imaging. Radiology. 2003;227(2):593–600.
19. Wintermark M, Sesay M, Barbier E, Borbély K, Dillon WP, Eastwood JD, et al. Comparative overview of brain perfusion imaging techniques. Stroke. 2005;36(9):83–99.
20. Bruening R, Kwong KK, Vevea MJ, Hochberg FH, Cher L, Harsh GR 4th, et al. Echo-planar MR determination of relative cerebral blood volume in human brain tumors: T1 versus T2 weighting. AJNR Am J Neuroradiol. 1996;17(5):831–40.
21. Chen F, Suzuki Y, Nagai N, Peeters R, Coenegrachts K, Coudyzer W, et al. Visualization of stroke with clinical MR imagers in rats: a feasibility study. Radiology. 2004;233:905–11.
22. Chen F, Suzuki Y, Nagai N, Sun X, Coudyzer W, Yu J, et al. Delayed perfusion phenomenon in a rat stroke model at 1.5 T MR: An imaging sign parallel to spontaneous reperfusion and ischemic penumbra? Eur J Radiol. 2007;61:70–8.
23. Fan G, Zang P, Jing F, Wu Z, Guo Q. Usefulness of diffusion/perfusion-weighted MRI in rat gliomas: correlation with histopathology. Acad Radiol. 2005;12(5):640–51.
24. van Osch MJ, van der Grond J, Bakker CJ. Partial volume effects on arterial input functions: shape and amplitude distortions and their correction. J Magn Reson Imaging. 2005;22(6):704–9.
25. Wada Y, Hara T, Miyati T. Basic assessment of the CNR measurement method of MRI system in phantom—suggestion for improvement in the CNR evaluation method. Nippon Hoshasen Gijutsu Gakkai Zasshi. 2008;64(2):268–76.
26. Ogura A, Maeda F, Miyai A, Hongoh T. Accuracy of contrast-to-noise ratio measurement for magnetic resonance clinical images. Nippon Hoshasen Gijutsu Gakkai Zasshi. 2004;60(11):1543–9.
27. Miyati T. Image quality assessment in magnetic resonance imaging. Nippon Hoshasen Gijutsu Gakkai Zasshi. 2002;58(1):40–8.
28. Wu O, Ostergaard L, Weisskoff RM, Benner T, Rosen BR, Sorensen AG. Tracer arrival timing-insensitive technique for estimating flow in MR perfusion-weighted imaging using singular value decomposition with a block-circulant deconvolution matrix. Magn Reson Med. 2003;50:164–74.
29. Besselmann M, Liu M, Diedenhofen M, Franke C, Hoehn M. MR angiographic investigation of transient focal cerebral ischemia in rat. NMR Biomed. 2001;14(5):289–96.
30. Bloom AS, Tershner S, Fuller SA, Stein EA. Cannabinoid-induced alterations in regional cerebral blood flow in the rat. Pharmacol Biochem Behav. 1997;57(4):625–31.
31. Shockley RP, LaManna JC. Determination of rat cerebral cortical blood volume changes by capillary mean transit time analysis during hypoxia, hypercapnia and hyperventilation. Brain Res. 1998;454(1–2):170–8.
32. Meier P, Zierler KL. On the theory of the indicator-dilution method for measurement of blood flow and volume. J Appl Physiol. 1954;6:731–44.
33. Johansson E, Månsson S, Wirestam R, Svensson J, Petersson JS, Golman K, et al. Cerebral perfusion assessment by bolus tracking using hyperpolarized 13C. Magn Reson Med. 2004;51(3):464–72.
34. Enmi J, Hayashi T, Watabe H, Moriwaki H, Yamada N, Iida H. Measurement of cerebral blood flow with dynamic susceptibility contrast MRI and comparison with O-15 positron emission tomography. Int Congr Ser. 2004;1265:150–8.
35. Calamante F, Vonken EJ, van Osch MJ. Contrast agent concentration measurements affecting quantification of bolus-tracking perfusion MRI. Magn Reson Med. 2007;58:544–53.
36. Grandin CB, Bol A, Smith AM, Michel C, Cosnard G. Absolute CBF and CBV measurements by MRI bolus tracking before and after acetazolamide challenge: repeatability and comparison with PET in humans. Neuroimage. 2005;26:525–35.
37. Kuhl CK, Träber F, Schild HH. Whole-body high-field-strength (3.0-T) MR imaging in clinical practice. Part I. Technical considerations and clinical applications. Radiology. 2008;246(3):675–96.
38. Jezzard P, Clare S. Sources of distortion in functional MRI data. Hum Brain Mapp. 1999;8(2–3):80–5.
39. Mayer D, Zahr NM, Adalsteinsson E, Rutt B, Sullivan EV, Pfefferbaum A. In vivo fiber tracking in the rat brain on a clinical 3T MRI system using a high strength insert gradient coil. Neuroimage. 2007;35(3):1077–85.
40. Graf H, Martirosian P, Schick F, Grieser M, Bellemann ME. Inductively coupled rf coils for examinations of small animals and objects in standard whole-body MR scanners. Med Phys. 2003;30(6):1241–5.